Journal of Magnetic Resonance 273 (2016) 113–123

Contents lists available at ScienceDirect

Journal of Magnetic Resonance

journal homepage: www.elsevier.com/locate/jmr

Development of ultrafast UTE imaging for granular systems

Hilary T. Fabich [a], Andrew J. Sederman [a], Daniel J. Holland [b,*]

[a] Department of Chemical Engineering and Biotechnology, University of Cambridge, New Museums Site, Pembroke Street, Cambridge CB2 3RA, United Kingdom
[b] Department of Chemical and Process Engineering, University of Canterbury, Private Bag 4800, Christchurch, New Zealand

ARTICLE INFO

Article history:
Received 27 September 2016
Revised 27 October 2016
Accepted 27 October 2016
Available online 29 October 2016

Keywords:
MRI
Ultrashort echo time
UTE
Granular flow
Rapid MRI

ABSTRACT

Ultrashort echo time (UTE) imaging is commonly used in medical MRI to image 'solid' types of tissue; to date it has not been widely used in engineering or materials science, in part due to the relatively long imaging times required. Here we show how the acquisition time for UTE can be reduced to enable a preliminary study of a fluidized bed, a type of reactor commonly used throughout industry containing short T_2^* material and requiring fast imaging. We demonstrate UTE imaging of particles with a T_2^* of only 185 μs, and an image acquisition time of only 25 ms. The images are obtained using compressed sensing (CS) and by exploiting the Hermitian symmetry of *k*-space, to increase the resolution beyond that predicted by the Nyquist theorem. The technique is demonstrated by obtaining one- and two-dimensional images of bubbles rising in a model fluidized bed reactor.

1. Introduction

Magnetic resonance (MR) is a powerful tool for studying optically opaque systems in medicine as well as engineering and materials science. However, it is often regarded as having poor temporal and spatial resolution, especially when used to study materials that exhibit very short T_2^* such as very viscous or rigid materials, or materials containing many solid-fluid interfaces. In engineering it is important to be able to image a large range of materials, including such short T_2^* systems, and to obtain images rapidly as the evolution of many of these systems takes place on a time scale below that accessible to traditional MR imaging. Here, one-dimensional volume averaged images and two-dimensional slice selective images, both based on ultrashort echo time (UTE) [1], are demonstrated. The images are reconstructed with a compressed sensing (CS) approach to help address limitations in temporal and spatial resolution. To demonstrate the techniques, images of bubbles rising freely in a gas-solid fluidized bed are obtained.

The gas-solid fluidized bed is a common process in chemical engineering whereby an upward flow of gas passes through a bed of fine (~1 mm) solid particles. When the drag force, exerted by the rising gas, on the particles is sufficient to support the weight of the particles, the particles will begin to behave like a fluid. When the gas flow is increased further, the bed will go into a bubbling state [2–4]. Fluidized bed reactors are used in industrial processes as the motion of bubbles enhances mixing in the system. Understanding the dynamics of these bubbles is critical when designing fluidized beds. However, owing to their opacity, MRI is one of the few techniques that can be used to study the internal dynamics of a bed [5]. Bubbles rise at approximately 0.1–0.3 m s^{-1}, making it necessary to image on a timescale of approximately 25 ms in order to capture rising bubbles [6]. This timescale is fast for conventional MRI imaging, especially of the short T_2^* material (typically $T_2^* < 1$ ms) used in a fluidized bed.

In previous MRI studies, images of rising bubbles in fluidized bed reactors have been acquired using fast low angle shot (FLASH) [6,7]. FLASH images were acquired in 25 ms with a resolution of 1.7 mm × 3.4 mm and a slice thickness of 5 mm. FLASH uses a small tip angle and is heavily T_2^* weighted which limits the signal to noise ratio (SNR), and hence resolution, when imaging samples with very short T_2^* times. Although these studies were able to show bubbles, the low spatial resolution, both in-plane and through plane, limited the conclusions that could be drawn. In addition to FLASH, there are other techniques that have been optimized to rapidly acquire images such as echo planar imaging (EPI) [8] and rapid acquisition with relaxation enhancement (RARE) [9]. However, EPI is limited to systems with relatively long T_2^* relaxation times, 5–10 ms, and RARE suffers from motion artifacts at velocities typically present in fluidized beds. Other techniques have been developed to acquire data from "more solid" materials such as single point imaging (SPI). However, even with fast versions of SPI, such as single point ramped imaging with T_1 enhancement (SPRITE) [10], acquisition times can be 10 s or more which is prohibitively long for studying many dynamic systems [11]. Where

* Corresponding author.
E-mail address: daniel.holland@canterbury.ac.nz (D.J. Holland).

http://dx.doi.org/10.1016/j.jmr.2016.10.016
1090-7807/

slice selection is not required, techniques such as sweep imaging with Fourier transform (SWIFT) [12] and zero echo time (ZTE) [13] can be used to image short T_2 and T_2^* systems. These techniques are usually used to acquire data in three dimensions and cannot be used with slice selection. Whilst three-dimensional images would provide further information about bubble motion in a sample, at present the acquisition time is too long to acquire 3D images of bubbles rising in a fluidized bed.

UTE is a slice selective, two-dimensional imaging technique that is well suited to short T_2 and T_2^* systems. UTE is well established in medical MRI for imaging short signal lifetime tissues such as cartilage, cortical bone, and teeth [14–16]. We have recently demonstrated the applicability of UTE in materials science and engineering by acquiring an image of cork which has a T_2^* of 120 μs [17]. UTE is advantageous for short T_2^* materials because the signal is acquired as a free induction decay (FID), rather than an echo. Thus, UTE has been demonstrated with an 8 μs dephasing time, or "echo time" [18], where in this sequence the "echo time" is defined as the time between the end of the radiofrequency (r.f.) pulse and the beginning of the data acquisition. The short effective echo time accommodates an increase in the spatial resolution that can be achieved by maximizing the SNR and extent of *k*-space sampled.

Dynamic images are not generally acquired using UTE. In the medical context, images of both long and short lifetime species are often required. Therefore, UTE is either implemented with an inversion pulse to null long T_2 components in systems where T_1 is approximately equal to T_2 leaving only short T_2 components to be imaged, or with a difference imaging approach, whereby the final image is obtained by subtracting a T_2 weighted image from a UTE image [19]. In both cases, the images take at least several seconds to acquire. In materials science and engineering applications, however, it is common for only short T_2^* components to be present, and dynamic images are often required. In this work, we develop and demonstrate a fast imaging technique based on UTE for use in engineering applications.

There are two common methods for reducing MRI acquisition time that can be combined with UTE: using small tip angles with reduced recycle time and reducing data sampling. Using a small tip angle for the excitation pulse, as is done in FLASH, allows the delay between excitations to be reduced. A short delay between excitations can dramatically decrease the total time for image acquisition. Image acquisition times can be reduced further by reducing the number of excitations which will, in turn, reduce the number of lines of data acquired in *k*-space. However, as may seem obvious, this will reduce the final image resolution, which may be undesirable depending on the application. More recently, compressed sensing (CS) has been introduced to MRI as a method of reducing acquisition time without decreasing spatial resolution [20–24]. CS is a rapidly developing field in mathematics, which uses the underlying, inherent structure in images to reconstruct them with less data than previously thought necessary. Depending on the nature of the image, images can be reconstructed with as little as 5% of the data indicated by the Nyquist sampling theory without introducing artifacts [24]. Therefore, if only the data required to reconstruct the image are acquired, the acquisition time can be reduced significantly. The key challenges to implementing CS are the correct choice of a domain in which the image can be represented sparsely and the correct image reconstruction algorithm [21,25].

In this paper we will describe a volume selective one-dimensional technique derived from UTE and ZTE, which enables the acquisition of one-dimensional images to characterize a dynamic system, specifically for calculating the average bubble rise velocity in a fluidized bed. In addition, we will detail developments to UTE, a slice-selective, two-dimensional technique, to allow for rapid imaging of short T_2^* material. Two-dimensional UTE images can be acquired in 25 ms with a spatial resolution of 1 mm × 1 mm × 2 mm. Preliminary experiments will show the potential for using UTE to image a fluidized bed, which is a heterogeneous, dynamic system, at higher spatial resolution than previously attainable without decreasing the temporal resolution.

2. Materials

Three samples are used to demonstrate rapid UTE. The first sample was composed of a bed of static *Nicotiana* seeds in a 23 mm inner diameter glass tube. The ^{1}H MR signal was measured from the oil in the seeds. The second sample was identical to the first but in addition had 5 mm diameter glass beads randomly distributed through the bed of seeds. No signal was obtained from the glass, therefore the second sample provided a static model of the type of image one might obtain in a bubbling fluidized bed. The third sample was a model fluidized bed. The bed consisted of a glass column with an inner diameter of 35 mm. At the base of the column was a porous, sintered glass distributor plate. The column was filled with *Nicotiana* seeds to a height of approximately 80 mm in the absence of gas flow. The bed was fluidized using air regulated to 1 barg at an ambient temperature of approximately 20 °C with the top of the bed open to the atmosphere. The velocity of air required to fluidize these particles, termed the minimum fluidization velocity, u_{mf}, was measured to be 0.10 m s^{-1} in this system. In order to image the bed in a bubbling state, the superficial velocity of the air within the fluidized bed was set to 0.15 m s^{-1}. The *Nicotiana* seeds were selected for their small diameter, 0.72 ± 0.12 mm, and relatively high sphericity with an aspect ratio of 0.80 ± 0.09. The relaxation times of the seeds are T_1 = 490 ms, T_2 = 25 ms, and T_2^* = 185 μs.

3. Methods

All experiments were performed using a Bruker AV400 spectrometer, operating at a ^{1}H resonance frequency of 400.23 MHz. The magnetic field used in these studies is stronger than in previous work [7], which was 199.7 MHz. The magnetic susceptibility is exaggerated at the higher field strength, however, the higher magnetic field will allow for an increased SNR and for higher resolution images to be acquired. A three-axis, shielded gradient system with a maximum strength of 30.6 G cm^{-1} was used for gradient encoding, and a 38 mm diameter birdcage r.f. coil was used for excitation and detection of the signal.

3.1. Reference MR imaging

Spin echo images of static samples are used as reference images to demonstrate the accuracy of the UTE images. The spin echo images were only used to image the static samples of *Nicotiana* seeds as they cannot be acquired sufficiently quickly to image bubbles in a fluidized bed. One-dimensional (1D) spin echo images were volume averaged over the full imaging region and acquired with a resolution of 0.16 mm per pixel. Two-dimensional (2D) spin echo images were acquired with a resolution of 0.45 mm × 0.45 mm over a 30 mm × 30 mm field of view (FOV) for *xy* and 0.78 mm × 0.78 mm over a 50 mm × 50 mm FOV for *zy* images, both with a 2 mm slice thickness. The echo time for the sequence was 2.2 ms, the repetition time was 2 s and the images were acquired using a single scan over period of 120 s.

For a comparison with a traditional rapid imaging sequence, FLASH was used to image the static sample of *Nicotiana* seeds [7]. FLASH images were acquired with a resolution of 0.45 mm × 0.9 mm and a 2 mm slice thickness over a

30 mm × 30 mm FOV. The sequence was executed with a 45° tip angle, echo time of 1.1 ms, 2 s recycle time, and 1 scan allowing for direct comparison with UTE images. The acquisition time was approximately 30 s. In processing the image, a baseline correction was used to eliminate the DC offset observed as a result of the single scan.

3.2. UTE profiles for short T_2^* samples

One-dimensional profiles were acquired using a sequence derived from UTE and ZTE. This sequence was chosen as it allows for rapidly repeated acquisitions for relatively long T_1 samples (~500 ms) though is also suitable for samples with very short T_2^* relaxation times, such as the seeds imaged here. The sequence used to acquire 1D profiles is shown in Fig. 1. Data was acquired following a hard pulse with a delay of 10 μs between the hard pulse and the ramping of the imaging gradient. In traditional ZTE imaging the gradients are ramped and stabilized prior to the excitation of the sample. The delay between excitation and detection means that an additional excitation is needed to acquire the center of *k*-space. In UTE the gradients are ramped from zero during the acquisition. Here the UTE approach was used following the hard excitation. A gradient mapping technique was used to define the shape of the gradient trajectory [26] and aid in accurate reconstruction of the profile. Using the measured trajectory, the data acquired for the profile are re-gridded onto a regular Cartesian grid and Fourier transformed using a non-uniform fast Fourier transform (NUFFT) [27]. This 1D imaging sequence will be referred to as 1D UTE in this article.

To image the fluidized bed in this study, two excitations with a 10° tip angle are used. After each excitation there is a 10 μs delay before starting the data acquisition in the center of *k*-space to acquire half of the *k*-space points. The positive *k*-space points are acquired first using a positive gradient. A second r.f. pulse is then used to excite the sample again and this time a negative gradient is used to acquire the negative *k*-space points. The acquisition time of each profile, including both the positive and negative *k*-space acquisitions, is 2.3 ms with a delay of 2.8 ms between each profile giving a recycle time of 5.1 ms. During each acquisition, 512 points are acquired with a dwell time between each complex data point of 1 μs. To reconstruct the profiles, 505 points were used giving 1010 points for a single reconstruction. The reconstruction of the profiles was performed to give a nominal resolution of 0.16 mm for the profiles of the static sample and a nominal resolution of 0.5 mm was used for the profiles of the dynamic sample. Due to the buffer size of the spectrometer used, a maximum of 125 sequential profiles could be acquired before writing the data to the disk.

3.3. UTE images

Our previous publication detailed a method for implementation of UTE with gradient pre-equalization and compressed sensing where a UTE image was acquired in 500 ms [17]. This study shows further developments to traditional UTE imaging enabling sequential images to be acquired in 25 ms or 40 frames per second (fps). A temporal resolution of 40 fps makes it possible to acquire real-time images of bubbles rising in a fluidized bed.

A depiction of the UTE pulse sequence can be seen in Fig. 2. The r.f. excitation is a half-Gaussian shape, which has been modified using variable rate selective excitation (VERSE) [28]. VERSE effectively adds a ramp that gradually decreases the applied power to zero while keeping the integral of the r.f. pulse power equal to that of the original half-Gaussian shape. Using a half-Gaussian shape allows for elimination of the refocusing gradient which means that the effective echo time, or time between the end of the r.f. pulse and the beginning of the acquisition, can be minimized. The effective echo time is then determined by the ring down for the r.f. coil and spectrometer used. The first excitation occurs simultaneously with a positive slice selection gradient, G_s, and the second excitation with a negative slice selection gradient. After each excitation is an acquisition. The acquisitions from the positive and negative slice selections are added together to represent one, center-out, radially sampled line of data in *k*-space. The addition of the two acquisitions eliminates the imaginary component of the slice selection which arises from the half-Gaussian r.f. pulse shape [18]. Full details of our implementation of this sequence are given elsewhere [17]. In this work a 10 μs effective echo time (TE) is used to allow for ring down of the hardware, and a single, complex point in *k*-space is acquired every microsecond.

Images were acquired in *xy* and *zy* planes, where *z* corresponds to the vertical direction and the direction of the main magnetic field. The principles for implementing UTE images in *xy* and *zy* planes are the same. However, the gradients in the *x*, *y*, and *z* directions may behave differently. Therefore it is important to calibrate the slice selection and measure the trajectory separately for each image orientation. The slice selection gradient was modified independently in *z*, for *xy* images, and *x*, for *zy* images, using gradient pre-equalization [29] and the gradient trajectories were mapped in both *xy* and *zy* [26].

Radially sampled *k*-space data were re-gridded using NUFFT [27]. Compressed sensing image reconstruction was performed using the alternating direction method of multipliers (ADMM) with total variation as the sparsifying transform [21]. The reconstructed images were normalized using an image with no bubbles to correct for inhomogeneity in the r.f. coil.

For the stationary sample, UTE images were acquired with 64 center-out radial spokes. The images were reconstructed to 0.45 mm × 0.45 mm for *xy* and 0.78 mm × 0.78 mm for *zy* images, both with a 2 mm slice thickness. The UTE image of the stationary sample, used as a reference image, was acquired with a 153 μs

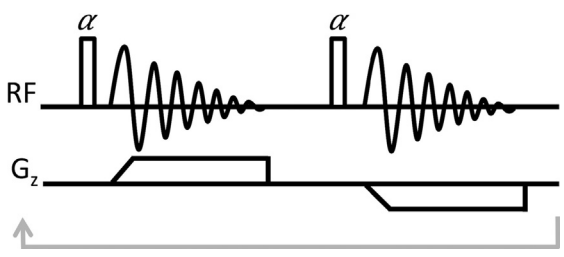

Fig. 1. One-dimensional UTE imaging sequence using a hard excitation, resulting in tip angle, α, and ramping the gradients from zero during the acquisition of the FID. The first excitation acquires data from the center to the positive edge of *k*-space and the second excitation from the center to the negative edge of *k*-space.

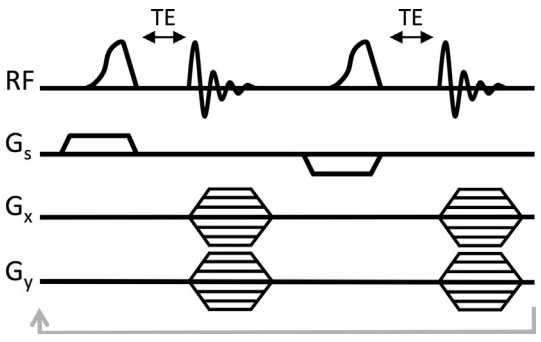

Fig. 2. Two dimensional UTE imaging sequence using a half-Gaussian - VERSE, slice selective, excitation. Two excitations and two acquisitions are used for each line acquired in *k*-space to produce a Gaussian shaped slice selection. Simultaneous ramping of *x* and *y* gradients produces a center-out, radial sampling pattern.

excitation ramped from maximum power to zero over 50 μs. A 45° tip angle was used for excitation and a 10 μs delay was set as the effective echo time. The recycle time, including excitations for both positive and negative slice selection, was 2 s leading to a 120 s acquisition.

3.4. UTE slice offset

The ability to define a slice offset is a necessity in many MRI applications. If the gradient during the excitation is constant, the slice can be offset simply by varying the frequency of the excitation pulse. However, the slice selection gradient in UTE ramps from its maximum value to zero during the excitation. Therefore the frequency of the pulse must change to match the changing gradient strength. This slice selection is illustrated in Fig. 3. The frequency is controlled by changing the phase during the excitation according to:

$$B_{1,n}(t) = B_1(t)\exp\left(i\gamma \int_t^{t_{end}} \boldsymbol{G}_s(\tau) z d\tau\right) \quad (1)$$

where B_1 is the original amplitude of the pulse, z is the desired slice offset, and $\boldsymbol{G}_s(\tau)$ is the slice gradient [18]. By changing the phase of the r.f. pulse according to Eq. (1), the effective slice position is held constant as the gradient varies. The changing phase is observed most clearly near the end of the excitation in Fig. 3. For each desired slice offset, an r.f. pulse is defined for the positive and negative slice selection gradients. The amplitude of each pulse is the same, but the phase of the pulse changes over time such that the correct slice position is chosen.

3.5. UTE rapid acquisition

As noted in the introduction, one of the commonly cited limitations in MRI is the long acquisition time required, making it unsuitable for acquiring data from rapidly evolving systems. With the use of CS, the amount of data needed to reconstruct an image is significantly reduced and thus the amount of time needed to acquire the data for the image is reduced.

In previous UTE experiments spokes have been equally distributed around k-space. However, it is known that half of k-space is the Hermitian conjugate of the other half for purely real images [30,31]. Therefore, theoretically, it is only necessary to acquire one half of k-space to reconstruct an image. In practice, Hermitian symmetry is typically a poor assumption as there is dephasing due to motion in the sample as well as some uncertainty over the exact location of the center of k-space [30,31]. However, in the application presented in this work, the phase shift is not significant. When using a spin echo or gradient echo image, a phase variation may originate from the assumption that the signal is acquired at $k = 0$, which is not strictly true. Using UTE, the center of the 'echo' is acquired as the gradient ramps after the acquisition starts. The phase shift in conventional imaging may also be amplified due to motion occurring over the relatively long acquisition times required. Due to the short signal lifetime of the sample with UTE, there is very little motion during the acquisition of each half echo. These two factors enable accurate images to be acquired from a half k-space acquisition with UTE.

A UTE image with 64 center-out radial spokes was used as a reference image for comparison with increasingly rapidly acquired images. A schematic of the acquired k-space trajectory is shown in Fig. 4a. With a reduced tip angle of 10° in our experiments, the recycle time can be reduced from 2 s to 2.7 ms and the 64 spoke image is acquired in approximately 170 ms, rather than 120 s. In addition, by acquiring only 16 spokes evenly distributed across k-space, as shown in Fig. 4b, an image is acquired in approximately 40 ms. Using Hermitian symmetry, only nine spokes, covering half of k-space are required, as shown in Fig. 4c, therefore an image is acquired in approximately 25 ms. A temporal resolution of 25 ms is of the time scale necessary to capture dynamic processes, such as bubbles rising in a fluidized bed.

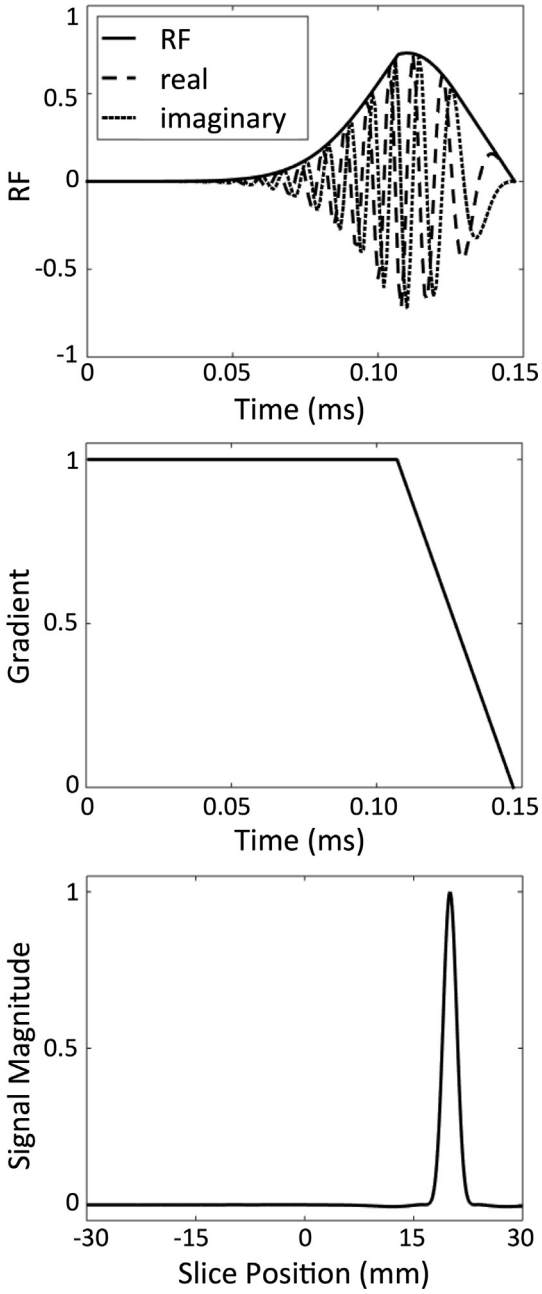

Fig. 3. r.f. and gradient input for excitation pulse used in UTE when exciting a slice at 20 mm. The frequency of the r.f. pulse varies as the slice selection gradient ramps to zero.

4. Results and discussion

To verify the accuracy of the 1D and 2D UTE techniques, the UTE acquisitions are first compared with a standard spin-echo technique on static samples. The acquisition time of the UTE techniques are then reduced such that they can be used to a model dynamic systems. The 1D images and rapidly acquired 2D images are then

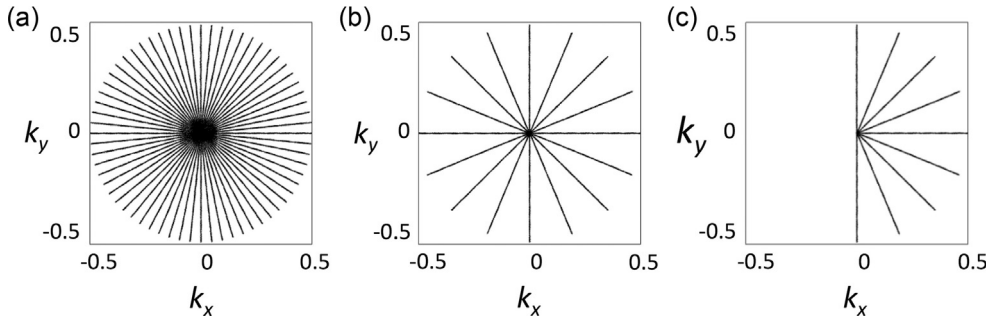

Fig. 4. *k*-space sampling trajectories (a) 64 spoke (b) 16 spoke (c) 9 spoke.

used to observe a model system: gas bubbles freely rising in a fluidized bed.

4.1. Method development

The volume averaged, 1D UTE sequence is implemented first. Fig. 5 shows 1D profiles acquired of two stationary samples using a spin echo sequence and the 1D UTE sequence described here. Fig. 5a shows a homogeneous sample of *Nicotiana* seeds in a stationary fluidized bed. The profiles observed with the two techniques are in good agreement. On the left hand side of both profiles there is a sharp decrease in signal intensity. This sharp change in signal intensity corresponds to the *Nicotiana* seeds resting on the glass distributor plate. No signal is obtained from the glass. The imaging region, or the region with signal, is shown to be similar in length. The difference between the two profiles arises on the right hand side. Though both profiles show a "bump" in signal, the feature is more exaggerated in the 1D UTE profile. The feature is likely due to inhomogeneity in the r.f. coil and may be more exaggerated in the 1D UTE profile due to the small tip angle used in UTE and therefore different spin manipulation between the 10° excitation in UTE and the 90–180° degree sequence used for the spin echo. The re-gridding process used to reconstruct the profile may also add some discrepancies. Although the general shape of both profiles is the same, the 1D UTE profiles have a noisier baseline as is expected due to the small excitation angle used. The apparent signal below the distributor plate is likely due to imperfect re-gridding of the data points onto a Cartesian plane. Overall, the UTE and spin echo profiles show strong similarities and the differences are considered negligible for the current application.

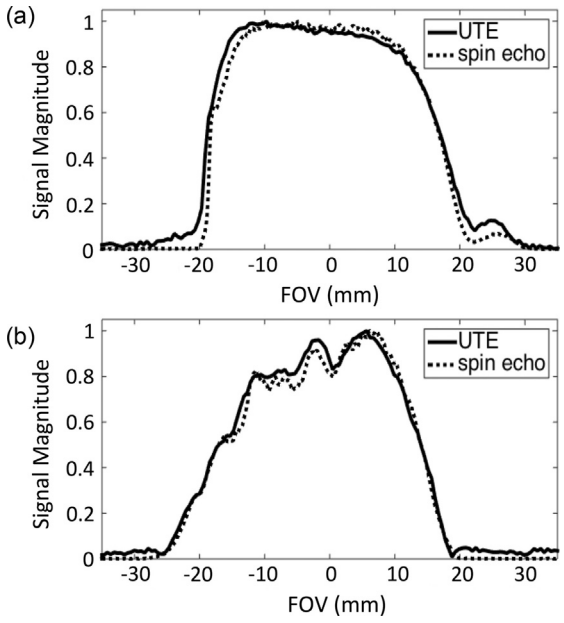

Fig. 5. 1D profiles along the *z*-axis comparing UTE and spin echo sequences for stationary samples of *Nicotiana* seeds. (a) UTE and spin echo profiles of a stationary fluidized bed. (b) UTE and spin echo profiles of 5 mm glass beads randomly distributed in *Nicotiana* seeds. The profiles were averaged over the whole *xy*-plane with a *z*-axis resolution of 0.16 mm per pixel.

Fig. 5b shows a similar sample of seeds to that imaged in Fig. 5a, however, this sample also contains 5 mm diameter glass beads which give no signal. The glass beads are distributed randomly throughout the sample. There is a reduction of the signal wherever the glass beads are located along the *z*-axis of the sample. The reduction in signal is similar to that seen from bubbles in a fluidized bed, making this sample a static model of the type of image expected for a bubbling fluidized bed. Overall the spin echo and the UTE profile are in very good agreement. The UTE profile uses only a 10° r.f. excitation resulting in a slightly noisier image than the spin echo technique. There is also a slight blurring observed in the UTE profile which is likely due to imperfections in the measured gradient trajectory. By comparing the UTE and spin echo images, it is estimated that there is blurring in the UTE images over 2 or 3 pixels, or 0.5 mm. Thus, the UTE profiles enable rapid imaging of dynamic samples with a short T_2^* relaxation time at a resolution of 0.5 mm, or better.

Two-dimensional images of the glass beads in *Nicotiana* seeds, were acquired using both spin echo and 64 spoke UTE imaging sequences, as shown in Fig. 6. Spin echo images are shown in Fig. 6a–c; Fig. 6d–f shows the same images acquired with a UTE pulse sequence. The *zy* images in Fig. 6a and d both show the same low signal intensity regions located mostly near the bottom of the imaging region. These dark regions correspond to the slice passing through glass beads, which give no NMR signal. The signal intensity distribution in both Fig. 6a and d is similar, indicating that the UTE acquisition and image reconstruction has been performed correctly. Similarly, the *xy* slices shown in Fig. 6 are well matched. This confirms the accuracy of the r.f. pulses defined to give a slice offset, as shown in Section 3.4.

Though the structure of the images compare well, there are two differences worth noting. Firstly, Fig. 6e and f both show lighter regions near the top bead in the image. These are not due to variations in packing density of the seeds directly, but rather are linked to small imperfections in the slice selection. These imperfections in the slice selection likely result from an interaction between the background magnetic field, which is distorted in the vicinity of the spheres, and the applied gradient. The effect is more pronounced with the UTE images than the spin echo images owing to the slice excitation continuing down to low gradient strengths with the UTE acquisition. Secondly, the UTE images appear to be more heavily smoothed. There are two possible reasons for this smoothing. The first is an effect of the short T_2^* inherent in the sam-

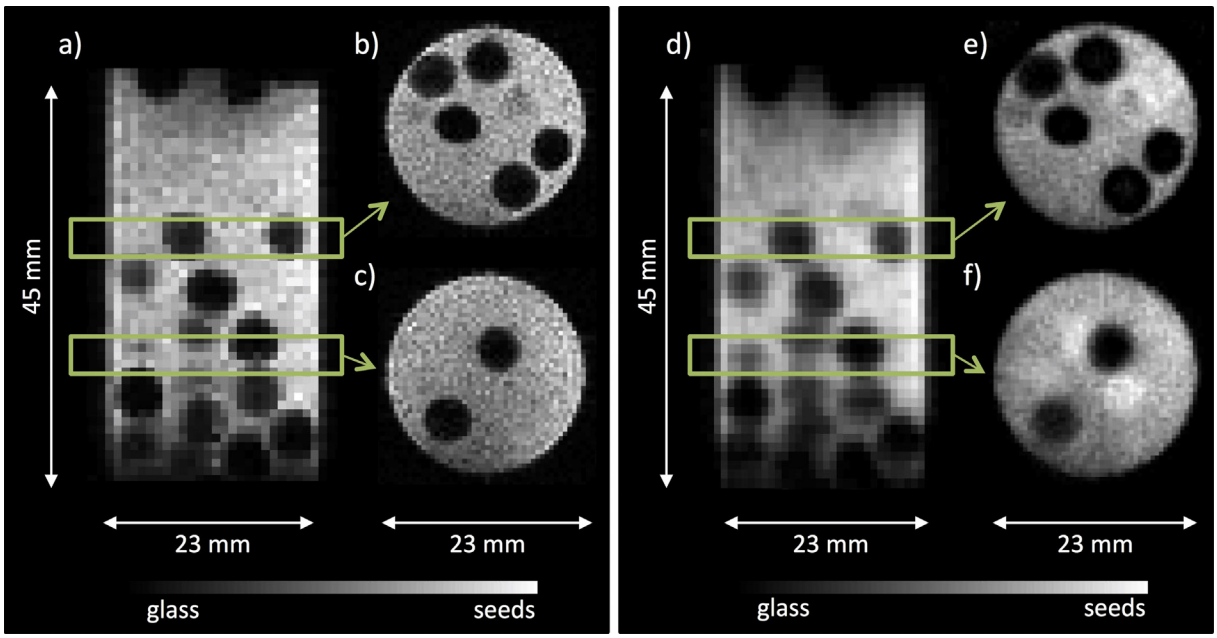

Fig. 6. Images of randomly distributed 5 mm diameter glass beads in *Nicotiana* seeds. (a)–(c) are spin echo images, (a) showing a *zy* image of the sample and (b) and (c) showing *xy* images at slice offsets of +5 mm, and −10 mm from the center of the imaging region respectively. (d)–(f) are UTE images of the same slices shown in (a)–(c). Both spin echo and UTE images are shown with a resolution of 0.45 mm × 0.45 mm over a 30 mm × 30 mm field of view (FOV) for *xy* and 0.78 mm × 0.78 mm over a 50 mm × 50 mm FOV for *zy* images, all with a 2 mm slice thickness.

ple. The rapid decay of the signal will weight data near the beginning of the acquisition and cause smoothing in the image. However, smoothing arising from the inherent T_2^* decay should affect both spin echo and UTE images approximately equally. The second, and more prevalent, effect is a function of the CS reconstruction. Using center-out, radial sampling means that the data is more heavily concentrated in the center of *k*-space. Using compressed sensing helps to reconstruct the detail that may otherwise be lost due to the sparse sampling at the edges of *k*-space. The glass beads are therefore imaged with essentially the same accuracy in both UTE and spin echo experiments. However, local variations in voidage on a length scale of the order of the particle size give the spin echo images a mottled appearance that is almost noise like. Structures such as this cannot be recovered by CS algorithms as they cannot be represented sparsely. Therefore the signal intensity in the dense regions of particles with the UTE images appears smooth, and not speckled as seen in the spin echo images. When the particles are moving, the local variations in voidage are rapidly averaged and will not be possible to resolve anyway.

The maximum achievable resolution of the sample can be estimated from:

$$\Delta x = \left(\frac{1}{\pi T_2^*}\right)\left(\frac{2\pi}{\gamma G}\right) \tag{2}$$

where γ is the gyromagnetic ratio of the nucleus and G is the acquisition gradient strength [32]. Given that the T_2^* of the *Nicotiana* seeds is 185 μs, and $G = 7$ G cm^{-1} the maximum achievable resolution will be 0.5 mm. The sharp edges for the region of signal between the two beads in the lower right hand portion of Fig. 6c and f, approximately one pixel across at the narrowest point, show that the resolution of the spin echo and UTE images is at least 0.5 mm × 0.5 mm. Thus, the results shown in Fig. 6 confirm that UTE can provide images close to the theoretical limit of spatial resolution for a frequency encoded acquisition and these images can be obtained for multiple slices at different spatial positions within the sample.

4.1.1. Comparison of UTE with FLASH

One rapid imaging sequence that has previously been used to study fluidized beds is FLASH. For comparison to the ultrafast UTE sequence, Fig. 7 shows a FLASH image of the stationary sample of *Nicotiana* seeds and glass beads. This is an *xy* image of the same plane as Fig. 6c and f using the same tip angle as used for UTE in Fig. 6f. The SNR for the UTE images in Fig. 6 is on the order of 100 and the SNR of the FLASH image is approximately four. The echo time for the FLASH image was 1.1 ms. Therefore, the signal is expected to have decayed to under 1% of the equilibrium intensity before the start of the acquisition, leading to a low SNR image. Reducing the recycle time to enable the study of bubbles in a fluidized bed would further reduce the SNR making it difficult to study dynamic processes in a fluidized bed with FLASH using this system. Previous dynamic imaging studies on fluidized beds using FLASH were performed on a 200 MHz magnet which would have given a longer signal lifetime than that of the 400 MHz spectrometer used for this study, and hence enabled higher SNR measurements albeit at lower spatial resolution.

4.1.2. Reduction in image acquisition time

The static sample containing 5 mm glass beads was used to investigate the fidelity of the image reconstruction relative to recycle time and the number of data points acquired, as shown in Fig. 8. All images in Fig. 8 are acquired through the center of the imaging region and are reconstructed to the same nominal resolution of 64 × 64 pixels, 0.45 mm × 0.45 mm and have a slice thickness of 2.4 mm. The UTE image in Fig. 8a is acquired with 64 spokes using a 45° tip angle for each excitation and a 2 s recycle time for a total image acquisition time of 120 s. This is used as the reference image for comparison with other images in Fig. 8. There are four glass beads clearly centered in the slice, a fifth which is clearly visible though not centered in the slice and four that are located along the edge of the slice, so there is signal throughout the bead though the shape can still be resolved. Fig. 8b is a 64 spoke acquisition of the same sample using a 10° tip angle for the excitation and a 2.7 ms recycle time meaning the acquisition time for this image

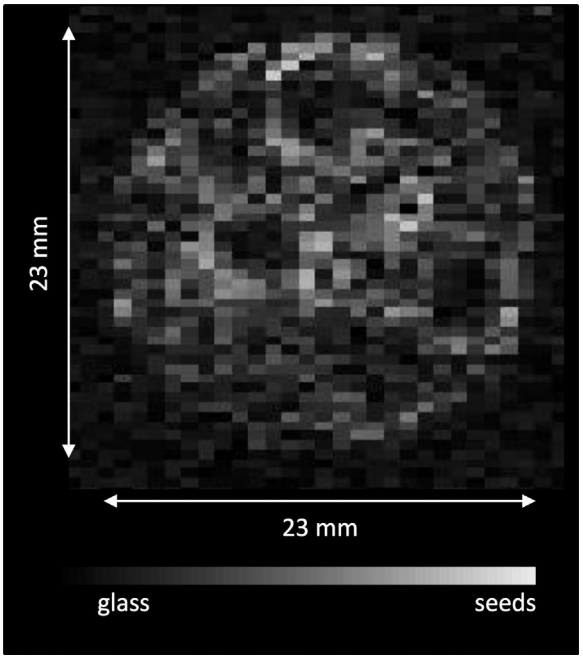

Fig. 7. FLASH image of *Nicotiana* seeds and glass beads for the sample shown in Fig. 6. The image is located at the same position and with the same slice thickness as is shown in Fig. 6c and f. The image was acquired with a resolution of 0.45 mm × 0.9 mm and a 2 mm slice thickness over a 30 mm × 30 mm FOV.

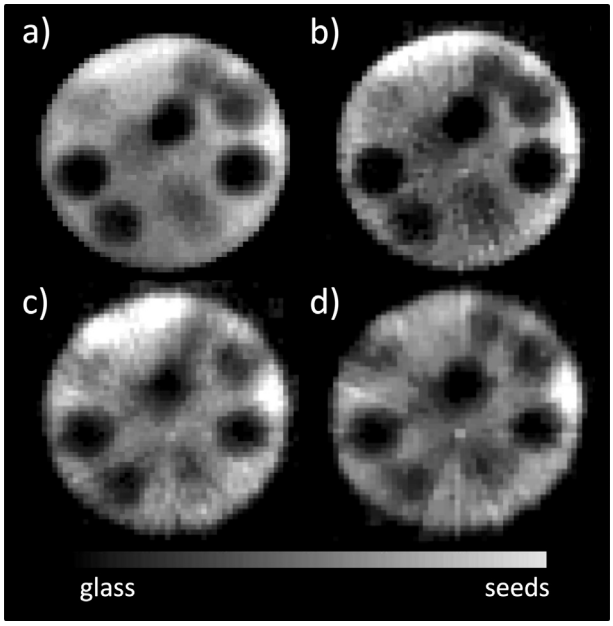

Fig. 8. Images showing the process for time reduction using UTE. (a) 64 spoke image using a 45° tip angle and 2 s recycle time, total acquisition time of 120 s. (b) 64 spoke image using a 10° tip angle and 300 μs recycle time, total acquisition time of 170 ms. (c) 16 spoke image using a 10° tip angle and 300 μs recycle time, total acquisition time of 40 ms. (d) 9 spoke image using a 10° tip angle and 300 μs recycle time, total acquisition time of 25 ms. All images are reconstructed to the same nominal resolution of 64 × 64 pixels, 0.45 mm × 0.45 mm and have a slice thickness of 2.4 mm.

is 170 ms. Using this low tip angle causes an approximately 70% reduction in the SNR. However, when comparing Fig. 8a and b, other than the visible reduction in the SNR, the sample is still clearly represented. All of the glass beads seen in Fig. 8a are also visible in Fig. 8b.

The acquisition time can be further reduced by reducing the total number of spokes acquired and relying more heavily on the CS reconstruction. Fig. 8c shows an image of the sample obtained using only 16 center-out radial spokes as shown in Fig. 4b. Reducing the number of spokes by a factor of four also reduces the total acquisition time by a factor of four from approximately 170 ms to approximately 40 ms. The image shown in Fig. 8c has an apparently lower resolution than that seen in Fig. 8a or b. The reduction in apparent resolution arises from the CS reconstruction. However, the structure of the sample is clearly represented and the significant features of the image, i.e. the location and size of the voids corresponding to the glass beads, are well resolved.

For a real image, half of *k*-space is the Hermitian conjugate of the other half, therefore only half of *k*-space needs to be acquired to reconstruct an image [31]. Fig. 8d is obtained by exploiting this principle and shows an image obtained from only 9 center-out spokes covering half of *k*-space as shown in Fig. 4c. Fig. 8d shows more pronounced radial artifacts than were seen in 8c and there is more smoothing, especially around the edge of the beads. Thus, the effective resolution is, as expected, lower than that in Fig. 8a. The reduction in resolution is largely due to noise in the measured data and imperfections in the measured *k*-space trajectory used for reconstruction. However, as with the 16 spoke reconstruction, the structure of the sample is still observed, especially for the beads that are located in-plane (i.e. for which the contrast is strongest).

Using a UTE, 9 spoke data acquisition the SNR and resolution both decrease. There is approximately a 70% reduction in signal from Fig. 8a–d though this is coupled with an increase in temporal resolution on the order of 1000. The resolution of Fig. 8d is most clearly observed while examining the edges of the beads when they are in close proximity. This sample contains features around 1 mm in length, such as the seeds located between the two in-plane beads in the bottom left of the image. These features are still visible indicating the true resolution of these images is 1 mm or better. This is a significant improvement on the previously obtainable images using FLASH which were acquired with a resolution of 1.7 mm × 3.4 mm with a 5 mm slice thickness [6]. The rapid UTE images acquired in 25 ms clearly represent the structure of the sample and can be applied in both *xy* and *zy* planes. The large number of features present in the images in Fig. 8 make it challenging sample to image. It is expected that many images, such as those in a fluidized bed, will contain significantly fewer features. Images with few features can be represented sparsely and hence the CS reconstruction is expected to perform at least as well as is seen with this challenging static sample.

4.2. Imaging of bubbles

4.2.1. Image normalization

The sample used for the demonstration of rapid imaging is a bubbling fluidized bed. The fluidized bed is 35 mm, inner diameter, meaning that the sample fills a larger portion of the r.f. coil than the 23 mm, inner diameter, stationary sample. The r.f. homogeneity is significantly reduced at the edges of the r.f. coil. When imaging a sample that fills the r.f. coil, the heterogeneity can be corrected for by normalizing the image to a homogeneous image of the sample or an image acquired with no bubbles rising through the sample. After normalizing the images they are masked to eliminate the noise around the edge of the sample, which is amplified as a result of the normalization. Fig. 9a shows an image of two bubbles rising in the fluidized bed prior to normalization and masking. Fig. 9b shows an image of a homogeneous sample, with no bubbles. Four bright patches around the edges of the image are seen clearly in the homogeneous image. These bright patches correspond to regions of higher r.f. intensity during the excitation, resulting in a heterogeneous signal across the sample. Fig. 9c shows the normal-

ized bubble image, which has been masked to 35 mm. In the normalized image the bright patches on the edges of Fig. 9a and b have been eliminated and the signal is more homogeneous across the image. All images of the fluidized bed were normalized in this way to eliminate unwanted variations in signal intensity arising from r.f. variations.

4.2.2. Volume averaged images of rising bubbles

In a bubbling fluidized bed, 1D profiles allow us to track the bubble rise velocity through the sample. As the bubbles rise through the fluidized bed, the reduction in signal corresponding to that bubble will be detected at progressively higher positions within the sample. Here blocks of a maximum of 125 profiles were acquired due to hardware constraints. Each profile is acquired over 2.3 ms with a total repetition time between profiles of 5.1 ms. Fig. 10 shows two blocks of 125 profiles. In this figure, the bubbles are indicated by the dark pixels in the images. The dark regions rise up from the distributor and allow us to track the bubbles as they rise through the sample.

The gradient of the bubble trajectories or the dark regions can be used to calculate the rise velocity of the bubbles in the fluidized bed. The gradient, and therefore rise velocity of the bubbles, is seen to increase with height above the distributor showing acceleration, as expected. It can also be seen from the profiles in Fig. 10 that some of the bubbles rise more quickly than others, a slow leading bubble is often followed by a rapidly rising, trailing bubble. The higher velocity of the trailing bubble means that the bubbles will coalesce. This is seen in the second set of profiles, Fig. 10b, where two dark lines meet (e.g. at ~150 ms and ~300 ms) and continue to rise as one. This process of coalescence is repeated four times in quick succession. From these profiles, the average bubble rise speed can be calculated to be approximately 0.1 m s^{-1} near the distributor and 0.3 m s^{-1} toward the top of the imaging region. However, one of the conclusions that can be taken from the 1D profiles is that the formation and rise velocity of the bubbles are unpredictable and that only a few bubbles will rise along the average trajectory.

4.2.3. Simultaneous tracking of bubble rise velocity and spatially resolved bubble behavior

Using a combination of 1D profiles in *z* and 2D images in the *xy* plane can help to develop a more complete understanding of the internal dynamics in a fluidized bed. Fig. 11 shows alternately acquired UTE profiles and images, numbered according to the order in which they were acquired. This allows for simultaneous tracking of the bubble rise velocity and the ability to observe the

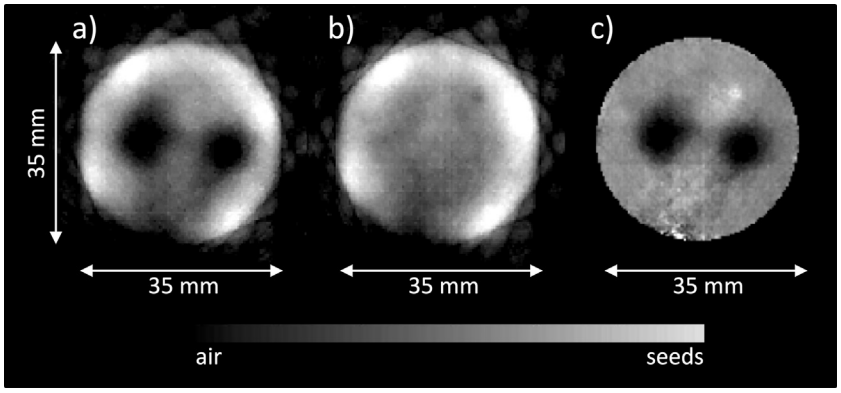

Fig. 9. Normalization of UTE images. (a) Is showing an *xy* image of two bubbles rising in a fluidized bed. (b) Is an image of a fluidized bed with no bubbles. (c) Is the normalized and masked image of the two bubbles shown in (a) normalized by the homogeneous image in (b). The resolution of the images is 0.5 mm × 0.5 mm with a slice thickness of 2 mm.

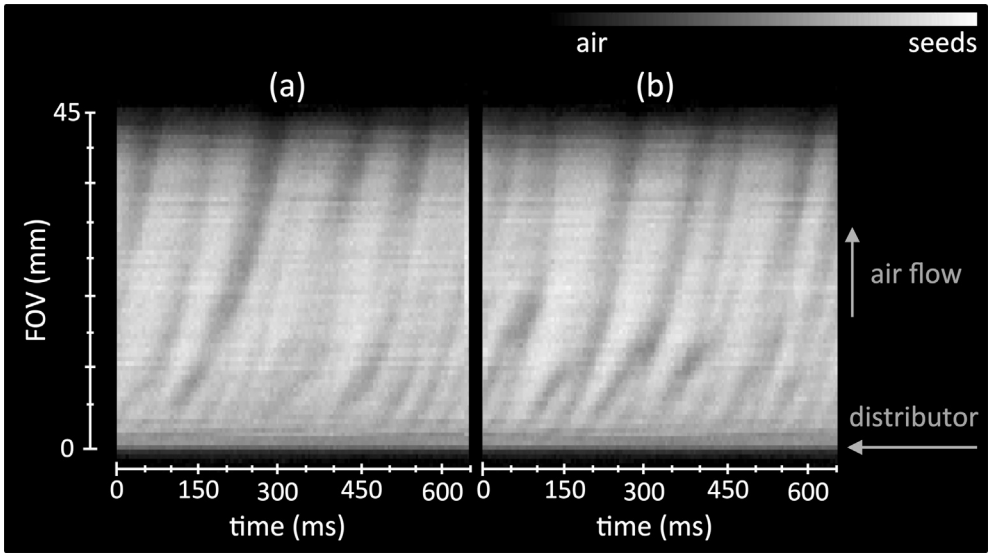

Fig. 10. Rapidly acquired 1D UTE profiles showing bubble trajectories in a bubbling fluidized bed. The spatial resolution of each profile is 0.5 mm.

bubbles in the *xy* plane. The signal-to-noise ratio for the acquisition of the profiles interleaved with the images was lower than for those profiles shown in Fig. 10. To reduce the influence of high frequency noise, the profiles were reconstructed with a Gaussian filter with standard deviation of 450,000 Hz. The 2D images were reconstructed with compressed sensing.

Fig. 11a shows profiles acquired of a bubbling fluidized bed. The red markers between each profile indicate the slice timing and location of the two-dimensional images in Fig. 11b. The temporal resolution for the profiles is significantly lower than shown in Fig. 10 as a two-dimensional image is acquired between each profile. However, the profiles in Fig. 11a clearly show two bubbles rising through the bed. The first profile shows one bubble approximately 25 mm above the distributor plate and a second bubble approximately 5 mm above the distributor plate. The second profile, acquisition 3, shows the first bubble at the top of the imaging region and the second bubble at approximately 8 mm above the distributor plate, just below the slice for the 2D images depicted in red.

Acquisitions 5, 7 and 9 show the first bubble accelerating and expanding vertically in size with the center at approximately 15 mm then 20 mm and finally 30 mm above the distributor plate.

Fig. 11b shows the two-dimensional images acquired between each profile. The first image, acquisition 2, is relatively uniform as is expected based on the location of the bubbles seen in the first profile. Some diagonal artifacts are seen in the image. These likely arise from noise in the measured data being amplified by the assumption of Hermitian symmetry in the reconstruction. These artifacts do not interfere with the analysis presented, as they can be distinguished clearly from the features of interest. Acquisition 4 shows a small bubble on the right hand side of the image. The second red marker in Fig. 11a shows this small bubble is the top of a bubble just moving into the frame. In acquisition 6, two bubbles are passing through the slice. The corresponding one-dimensional profiles show a reduction in signal in the profile, but this reduction in signal can only indicate the presence and approximate size of a bubble. The final image, acquisition 8, shows only one bubble in the left hand part of the image with a larger diameter than the corresponding bubble in the previous image. Using the profiles and images, it can be inferred that there were two bubbles, one rising just below the other in different lateral positions. The top of the first bubble was acquired in acquisition 4. Acquisition 6 shows a slice through a more central part of the bubble from acquisition 4 and through the upper region of a second bubble. The final image, acquisition 8 shows only the second bubble. This set of images show a "leading/trailing" bubble pattern where the bubbles are clearly separate, but too close together to be resolved using the profiles alone.

In addition to *xy* images, images in the *zy* plane can be used to track bubbles rising, as shown in Fig. 12. Each *zy* image is acquired in 25 ms and the images are acquired consecutively with no profiles. The images in Fig. 12 have been normalized to a homogeneous image of the sample. There is a bubble near the left hand side of the first image in Fig. 12. This bubble can be seen to rise through the sample in the next two images. The bubble is relatively circular in the first two images and is starting to form a flat bottom in the third image. The flat bottom may be an intermediate step in forming a bubble wake traditional of bubbles in fluidized beds [2,3].

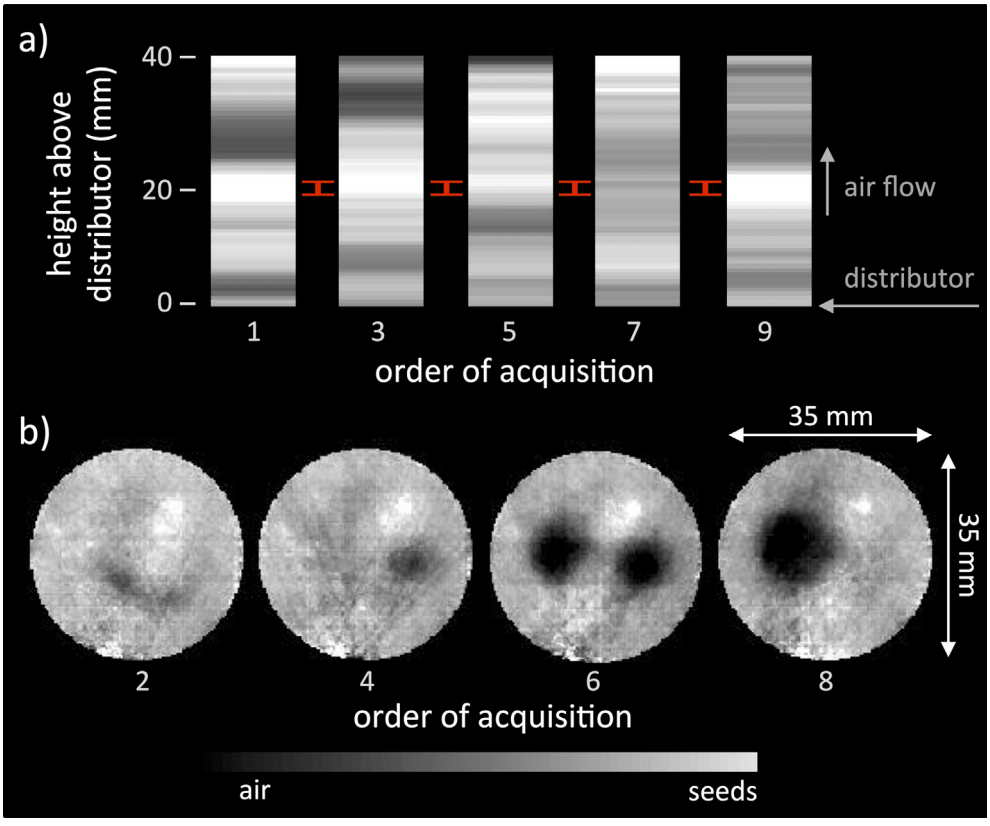

Fig. 11. (a) 1D profiles along the *z*-axis showing a bubble rising through the fluidized bed. The resolution of the profiles is 0.5 mm. The red markers indicate *xy* slice location, slice thickness and relative timing. (b) 2D *xy* images acquired between each profile in (a) showing two bubbles passing through the center of the imaging region. The resolution of the images is 0.5 mm × 0.5 mm with a slice thickness of 2 mm. (For interpretation of the references to color in this figure legend, the reader is referred to the web version of this article.)

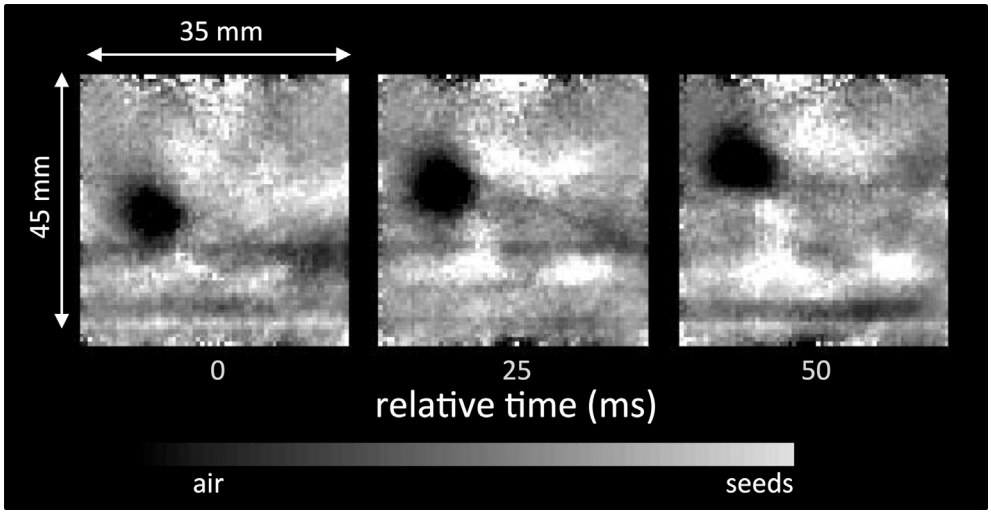

Fig. 12. Sequence of *zy* images, each acquired in 25 ms, showing a bubble rising in a fluidized bed. The resolution of the images is 0.5 mm × 0.5 mm with a slice thickness of 2 mm.

5. Conclusions

A rapid imaging technique has been developed based on the UTE pulse sequence originally developed for use in medical MRI. Spin echo images of a static sample are used as a reference to show that UTE can be used to acquire accurate images of a sample of *Nicotiana* seeds with a T_2^* of 185 μs. FLASH, a commonly used rapid imaging sequence, was shown to be unsuitable for imaging these samples. Using UTE, images of a static sample of *Nicotiana* seeds were obtained with a spatial resolution of 0.5 mm × 0.5 mm × 2 mm in 120 s. By using a small tip angle and a CS image reconstruction the image acquisition time was reduced to 25 ms, a factor of almost 5000. The reduction in acquisition time led to a slight blurring in the image, though an overall spatial resolution of 1 mm × 1 mm × 2 mm was still achieved. The potential for using this sequence to study bubbles rising in a fluidized bed, a rapidly evolving, optically opaque system is demonstrated. These types of images will be helpful in verifying and optimizing computational models of fluidized beds. In addition, UTE will be of use in studying many other systems relevant to engineering and materials science.

Acknowledgments

HTF would like to acknowledge the financial support of the Gates Cambridge Trust. All authors would like to acknowledge the financial support of the EPSRC (EP/K008218/1, EP/F047991/1 and EP/K039318/1).

Data shown in this publication and further data in support of the paper can be found at http://dx.doi.org/10.17863/CAM.6053.

References

[1] J.M. Pauly, S.M. Conolly, D.G. Nishimura, A. Macovski, Slice-selective excitation for very short T2 species, in: Proceedings of the 8th Annual Meetings, SMRM, Amsterdam, 1989, p. 28.
[2] D. Kunii, O. Levenspiel, Fluidization Engineering, Butterworth-Heinemann, Stoneham, 1991, http://dx.doi.org/10.1016/B978-0-08-050664-7.50003-2.
[3] J.F. Davidson, D. Harrison, Fluidised Particles, Cambridge University Press, Cambridge, 1963.
[4] J.S. Dennis, Properties of stationary (bubbling) fluidised beds relevant to combustion and gasification systems, in: F. Scala (Ed.), Fluidized Bed Technologies for Near-Zero Emission Combustion and Gasification, first ed., Woodhead Publishing, Philadelphia, 2013, pp. 77–146.
[5] M. Wang (Ed.), Industrial Tomography: Systems and Applications, first ed., Woodhead Publishing, Oxford, 2015, http://dx.doi.org/10.1016/B978-1-78242-118-4.00023-X.
[6] D.J. Holland, C.R. Müller, J.S. Dennis, L.F. Gladden, J.F. Davidson, Magnetic resonance studies of fluidization regimes, Ind. Eng. Chem. Res. 49 (2010) 5891–5899, http://dx.doi.org/10.1021/ie901450q.
[7] C.R. Müller, D.J. Holland, J.F. Davidson, J.S. Dennis, L.F. Gladden, A.N. Hayhurst, et al., Rapid two-dimensional imaging of bubbles and slugs in a three-dimensional, gas-solid, two-phase flow system using ultrafast magnetic resonance, Phys. Rev. E. 75 (2007) 020302, http://dx.doi.org/10.1103/PhysRevE.75.020302.
[8] P. Mansfield, Multi-planar image formation using NMR spin echoes, J. Phys. C Solid State Phys. 10 (1977) L55–L58, http://dx.doi.org/10.1088/0022-3719/10/3/004.
[9] J. Hennig, A. Nauerth, H. Friedburg, R.A.R.E. Imaging, A fast imaging method for clinical MR, Magn. Reson. Med. 3 (1986) 823–833, http://dx.doi.org/10.1002/mrm.1910030602.
[10] B.J. Balcom, R.P. MacGregor, S.D. Beyea, D.P. Green, R.L. Armstrong, T.W. Bremner, Single-point ramped imaging with T1 enhancement (SPRITE), J. Magn. Reson. 123 (1996) 131–134, http://dx.doi.org/10.1006/jmra.1996.0225.
[11] B. Blümich, NMR Imaging of Materials, Oxford University Press, Oxford, 2000.
[12] D. Idiyatullin, C. Corum, J.-Y. Park, M. Garwood, Fast and quiet MRI using a swept radiofrequency, J. Magn. Reson. 181 (2006) 342–349, http://dx.doi.org/10.1016/j.jmr.2006.05.014.
[13] M. Weiger, K.P. Pruessmann, MRI with zero echo time, Encycl. Magn. Reson. (2012) 311–321, http://dx.doi.org/10.1002/9780470034590.emrstm1292.
[14] M.D. Robson, G.M. Bydder, Clinical ultrashort echo time imaging of bone and other connective tissues, NMR Biomed. 19 (2006) 765–780, http://dx.doi.org/10.1002/nbm.
[15] M. Weiger, K.P. Pruessmann, A.-K. Bracher, S. Köhler, V. Lehmann, U. Wolfram, et al., High-resolution ZTE imaging of human teeth, NMR Biomed. 25 (2012) 1144–1151, http://dx.doi.org/10.1002/nbm.2783.
[16] J. Du, M. Carl, M. Bydder, A. Takahashi, C.B. Chung, G.M. Bydder, Qualitative and quantitative ultrashort echo time (UTE) imaging of cortical bone, J. Magn. Reson. 207 (2010) 304–311, http://dx.doi.org/10.1016/j.jmr.2010.09.013.
[17] H.T. Fabich, M. Benning, A.J. Sederman, D.J. Holland, Ultrashort echo time (UTE) imaging using gradient pre-equalization and compressed sensing, J. Magn. Reson. 245 (2014) 116–124, http://dx.doi.org/10.1016/j.jmr.2014.06.015.
[18] J.M. Pauly, Selective excitation for ultrashort echo time imaging, Encycl. Magn. Reson. 1 (2012) 381–388, http://dx.doi.org/10.1002/9780470034590.emrstm1271.
[19] J.E. Holmes, G.M. Bydder, MR imaging with ultrashort TE (UTE) pulse sequences: basic principles, Radiography 11 (2005) 163–174, http://dx.doi.org/10.1016/j.radi.2004.07.007.
[20] E.J. Candès, J. Romberg, T. Tao, Robust uncertainty principles: exact signal frequency information, IEEE Trans. Inf. Theory. 52 (2006) 489–509, http://dx.doi.org/10.1109/TIT.2005.862083.
[21] M. Benning, L. Gladden, D. Holland, C.-B. Schönlieb, T. Valkonen, Phase reconstruction from velocity-encoded MRI measurements - a survey of sparsity-promoting variational approaches, J. Magn. Reson. 238 (2014) 26–43, http://dx.doi.org/10.1016/j.jmr.2013.10.003.
[22] U. Gamper, P. Boesiger, S. Kozerke, Compressed sensing in dynamic MRI, Magn. Reson. Med. 59 (2008) 365–373, http://dx.doi.org/10.1002/mrm.21477.
[23] D.J. Holland, D.M. Malioutov, A. Blake, A.J. Sederman, L.F. Gladden, Reducing data acquisition times in phase-encoded velocity imaging using compressed

sensing, J. Magn. Reson. 203 (2010) 236–246, http://dx.doi.org/10.1016/j.jmr.2010.01.001.
[24] M. Lustig, D. Donoho, J.M. Pauly, Sparse MRI: the application of compressed sensing for rapid MR imaging, Magn. Reson. Med. 58 (2007) 1182–1195, http://dx.doi.org/10.1002/mrm.21391.
[25] J.A. Tropp, J.N. Laska, M.F. Duarte, J.K. Romberg, R.G. Baraniuk, Beyond Nyquist: efficient sampling of sparse bandlimited signals, IEEE Trans. Inf. Theory 56 (2010) 520–544, http://dx.doi.org/10.1109/TIT.2009.2034811.
[26] J.H. Duyn, Y. Yang, J.A. Frank, J.W. van der Veen, Simple correction method for k-space trajectory deviations in MRI, J. Magn. Reson. 132 (1998) 150–153, http://dx.doi.org/10.1006/jmre.1998.1396.
[27] J.A. Fessler, B.P. Sutton, Nonuniform fast Fourier transforms using min-max interpolation, IEEE Trans. Signal Process. 51 (2003) 560–574, http://dx.doi.org/10.1109/TSP.2002.807005.
[28] B.A. Hargreaves, C.H. Cunningham, D.G. Nishimura, S.M. Conolly, Variable-rate selective excitation for rapid MRI sequences, Magn. Reson. Med. 52 (2004) 590–597, http://dx.doi.org/10.1002/mrm.20168.
[29] F.G. Goora, B.G. Colpitts, B.J. Balcom, Arbitrary magnetic field gradient waveform correction using an impulse response based pre-equalization technique, J. Magn. Reson. 238 (2014) 70–76, http://dx.doi.org/10.1016/j.jmr.2013.11.003.
[30] E.M. Haacke, E.D. Lindskog, W. Lin, A. Fast, Iterative, partial-Fourier technique capable of local phase recovery, J. Magn. Reson. 92 (1991) 126–145, http://dx.doi.org/10.1016/0022-2364(91)90253-P.
[31] G. McGibney, M.R. Smith, S.T. Nichols, A. Crawley, Quantitative evaluation of several partial fourier reconstruction algorithms used in MRI, Magn. Reson. Med. 30 (1993) 51–59, http://dx.doi.org/10.1002/mrm.1910300109.
[32] P.T. Callaghan, Principles of Nuclear Magnetic Resonance Microscopy, Oxford University Press, Oxford, 1991.